Journal of Power Sources 205 (2012) 449–455

Contents lists available at SciVerse ScienceDirect

Journal of Power Sources

journal homepage: www.elsevier.com/locate/jpowsour

Effect of Mg-doping on the degradation of $LiNiO_2$-based cathode materials by combined spectroscopic methods

Shunsuke Muto[a,*], Kazuyoshi Tatsumi[a], Yuji Kojima[a], Hideaki Oka[b], Hiroki Kondo[b], Kayo Horibuchi[b], Yoshio Ukyo[b]

[a] Graduate School of Engineering, Nagoya University, Chikusa-ku, Nagoya, Aichi 464-8603, Japan
[b] Toyota Central R&D Laboratories Inc., Nagakute, Aichi 480-1192, Japan

ARTICLE INFO

Article history:
Received 24 November 2011
Received in revised form 4 January 2012
Accepted 11 January 2012
Available online 18 January 2012

Keywords:
Lithium ion secondary battery
Electrochemical impedance spectroscopy
Scanning transmission electron microscopy
Electron energy loss spectroscopy
Cathode
Degradation

ABSTRACT

The performance of a $LiNiO_2$-based cell has been shown to be significantly improved by Mg-doping of $LiNi_{0.8}Co_{0.15}Al_{0.05}O_2$ (Mg-doped NCA) cathode materials. In the present study, the effects of Mg-doping were examined by electrochemical impedance spectroscopy (EIS) and scanning transmission electron microscopy-electron energy loss spectroscopy. EIS analysis revealed that the activation energy of Mg-doped NCA for the charge-transfer reaction was larger than that of undoped NCA by a factor of ~10%; however, the charge-transfer resistance for Mg-doped NCA did not vary significantly with cycling, suggesting a different microstructure evolution compared to that of the undoped NCA. The spatial mapping of the product phases in the Mg-doped samples showed less degradation after charge–discharge cycling tests at 70 °C compared to that in the undoped samples. In addition, degraded regions observed near the surface of the primary active material particles were identified as an intermediate structure, containing tetrahedrally coordinated Ni in contrast to the NiO-like phase found in the undoped samples. These microstructural observations are consistent with the electrochemical measurements.

1. Introduction

Cathode materials are key components in rechargeable lithium-ion batteries, and have been studied intensively since the advent of high-energy-density $LiMO_2$ (M = Co, Ni) cathodes in 1980 [1] and the subsequent commercial success of $LiCoO_2$ cathode materials. Although $LiCoO_2$ is considered to be a well-established material in mobile applications, alternatives to $LiCoO_2$ have become necessary due to its high cost and toxicity in high-power and large-scale energy storage applications. $LiNiO_2$ [2–6] was a promising alternative to $LiCoO_2$, stimulating extensive studies on cationic substitution, including Co [7–9], Fe [10], Mn [11–13], Al [14,15], Mg [16–18], Co/Al [19–22], and Co/Mg [23,24], for Ni in an attempt to stabilize the layered structure of the material. Among the wide range of materials, $LiNi_{1-x-y}Co_xAl_yO_2$ (NCA), in which the stability is improved by Al doping, was the most successful alternative to $LiCoO_2$ due to the higher reversible capacity and better environmental compatibility. However, in automotive applications, degradation at elevated temperature (60–80 °C) was found to be a serious problem [6–15], such as capacity fading and impedance rise [25–28]. The capacity fading of the NCA battery was mainly attributed to the cathode material [29], though no significant changes could be detected by macroscopic analysis techniques, such as X-ray diffraction (XRD), due to their small volume fraction or poor ordering.

In order to provide more insight on degradation processes in NCA batteries at elevated temperature, we applied a statistical signal processing technique to spectrum imaging (SI) datasets obtained by scanning transmission electron microscopy (STEM) and electron energy-loss spectroscopy (EELS) to resolve the overlapping spectral components, thereby visualizing the spatial distribution of each different chemical state on a relative concentration map [30–32]. This method successfully revealed that a NiO-like phase was distributed near the surface of NCA particles after the charge–discharge cycling test at an elevated temperature, and that device degradation could be largely explained by the evolution of the NiO-like phase, particularly near the NCA particle surface [31,33]. In our series of studies, the "NiO-like" phase (or similarly "spinel-like" appearing below) refers to the local atomic configuration and chemical states probed by EELS, rather than to a long-range order having translational symmetry.

To improve the device stability, we proposed Mg-doped NCA ($LiNi_{0.75}Co_{0.15}Al_{0.05}Mg_{0.05}O_2$) as a cathode material [34]. This actually suppressed the capacity fading and increase in resistance during cycling at 60 °C. The increase in resistance of the NCA cell was attributable to the increasing impedance of the cathode [34].

* Corresponding author. Tel.: +81 52 789 5200; fax: +81 52 789 4684.
E-mail address: s-mutoh@nucl.nagoya-u.ac.jp (S. Muto).

0378-7753/$ – see front matter © 2012 Elsevier B.V. All rights reserved.
doi:10.1016/j.jpowsour.2012.01.071

We examined the state of Mg in $LiNi_{0.75}Co_{0.15}Al_{0.05}Mg_{0.05}O_2$ by neutron diffraction [34], EELS, XAFS, and first-principles theoretical calculations [35], and found that Mg is mainly substituted at the Ni site, and that Ni—O bonding around the dopant was significantly reinforced owing to a greater degree of ionic bonding.

Here, we examine how Mg-doping affects the local spatial and electronic structure of NCA cathodes in the cycling tests at 70 °C, using electrochemical impedance spectroscopy (EIS), STEM-EELS, and SI multivariate curve resolution (MCR) techniques, by comparing the obtained microscopic and macroscopic electrochemical measurements.

2. Experimental

2.1. Cell fabrication and test conditions

Cathode materials, $LiNi_{0.8-x}Co_{0.15}Al_{0.05}Mg_xO_2$ ($x = 0, 0.05$), were prepared by the co-precipitation method, followed by a solid-state reaction: A mixed hydroxide powder containing stoichiometric amounts of Ni, Co, Al and Mg was co-precipitated in an aqueous solution. Finally, the dried mixed hydroxide was sintered at 750 °C under an oxygen gas flow with 5% excess of lithium carbonate. The undoped ($x = 0$) and Mg-doped ($x = 0.05$) materials are herein referred to as NCA and Mg-doped NCA, respectively. The size of the primary particles ranges between 100 nm and 1 μm, agglomerated to form secondary particles of ~12 μm and ~7 μm on average for NCA and Mg-doped NCA, respectively.

Cell performance was examined using 18650-type (750 mAh) cylindrical cells with graphite as the anode material. The detailed cell fabrication procedure is described in Ref. [34]. The positive and negative electrodes were wound with a polyethylene separator and placed into a cylindrical cell case with 1 M $LiPF_6$ dissolved in an ethylene carbonate/dimethyl carbonate/ethyl methyl carbonate (3:4:3 in volume) mixed solvent. After several initial charge–discharge conditioning cycles, the high-temperature cycling test was carried out at a 2 C rate for 500 cycles, in the voltage range of 3.0–4.1 V, at 70 °C. The reversible cell capacity was measured by charging the cells under a constant voltage to 4.1 V and discharging them at a 0.1 C rate to 3.0 V at 20 °C before and after the cycling test. *I–V* resistance was obtained from the voltage response in relation to the direct current for 10 s at 20 °C [34].

After discharging to 3.0 V, the cell was disassembled in an Ar-filled glove box with great care to prevent a short circuit. A cell subjected only to the initial conditioning cycles was also disassembled in the same manner for comparison. The cathode samples were rinsed with dimethyl carbonate three times to completely remove residual electrolyte.

EIS was carried out using a three-electrode cell with a Solartron 1255WB frequency response analyzer [36]. The amplitude was 5 mV in the frequency range 0.01 Hz–100 kHz.

2.2. STEM-EELS spectrum imaging and analysis

A focused ion beam thinning technique was used to produce 100-nm-thick samples with an area of ~10 μm × 10 μm equivalent to the secondary particle size in the cathode. In the same manner as previous studies [33], STEM-EELS SI data were acquired at room temperature using a JEOL JEM2100 S/TEM for the low-loss region (including Li-K, Co- and Ni-$M_{2,3}$ absorption edges) and a JEM2100F S/TEM with the spherical aberration of the illumination system corrected for the high-energy region (including O-K, Co- and Ni-$L_{2,3}$ edges). Both machines are equipped with a Gatan Enfina 1000 spectrometer. Data pre-processing and MCR analysis procedures were also the same as previously reported studies [30–33].

Table 1
Capacity and *I–V* resistance of cells using NCA and Mg-doped NCA cathodes, before and after cycling. The capacity was normalized by the weight of the cathode material contained in the cylindrical cell. *I–V* resistance was calculated by the response of the cell voltage over 10 s to a constant current. All the data was obtained at 20 °C.

	Capacity (mAh g^{-1})		*I–V* resistance (10 s) (mΩ)	
	Fresh	Cycled	Fresh	Cycled
$LiNi_{0.8}Co_{0.15}Al_{0.05}O_2$ (NCA)	169.3	132.0 (−22.0%)	51.8	79.7 (+53.9%)
$LiNi_{0.75}Co_{0.15}Al_{0.05}Mg_{0.05}O_2$ (Mg-doped NCA)	147.9	125.4 (−15.2%)	53.7	69.4 (+29.2%)

2.3. Theoretical O-K ELNES calculations

We calculated the theoretical electron energy-loss near the edge structure (ELNES) of the transition from the O 1s to O 2p unoccupied states using the augmented plane wave plus local orbital (APW + lo) band method, within the generalized gradient approximation (GGA; WIEN2k simulation package) [37], to compare the relative peak intensities and positions of the experimental and theoretical spectra. For Ni *d* states, we adopted a Hubbard-type orbital-dependent interaction, in a similar manner to Refs. [32,35]. Supercells containing 56–128 atoms were used, with a core hole introduced explicitly at the excited atom. Prior to spectral calculations, structural parameters were optimized using the projected augmented wave method (VASP simulation package) [38]. For optimization, the Hubbard parameter, U_{eff}, was set to 6.7 eV (GGA + *U*), which was obtained for $LiNiO_2$ by a self-consistent linear-response procedure [39]. The atom positions were freely relaxed under the constraint of the given symmetry of the supercell, within the fixed supercell size, until the residual forces were reduced to less than 0.05 eV $Å^{-1}$. The final ELNES spectrum was broadened by a Gaussian function with a full width at half-maximum of 1.5 eV. In the spectral calculations, U_{eff} was set to 2.0 eV because the peak energy positions in the O-K ELNES of NiO calculated using this value were most consistent with the experimental values of a previously reported study [40].

3. Results and discussion

3.1. Cell performance

The effect of Mg-doping on the cycling durability at 70 °C showed the same trend as that at 60 °C [34]. The low-rate capacity and *I–V* resistance of the cells before and after the cycling test are summarized in Table 1. The cyclability of the cell was improved by Mg-doping; however, the initial cell capacity of Mg-doped NCA was smaller than that of undoped NCA. Conversely, the *I–V* resistance of the NCA cell increased by 53.9% after cycling, while Mg-doping suppressed the increase in cell resistance to only 29.2%.

3.2. EIS measurements

Nyquist plots of both the NCA and Mg-doped NCA are shown in Fig. 1(a) and (b), respectively. All Nyquist plots show two successive convex arcs, each corresponding to the high (left arc) and low (right arc) frequency ranges, respectively. The right arc in the low frequency range (~1 Hz) corresponds to the charge-transfer resistance of the cathode, since the diameter of the right arc showed clear correlation with electrode potential. In contrast, the diameter of the high frequency part (left arc) was independent of the cathode potential, as examined in the previous paper [29]. We presume that the left arc could comprise multiple effects such as the resistances of the lithium counter electrode and solid-electrolyte interphase (SEI) of cathode. Therefore, we herein focus on only the right arc.

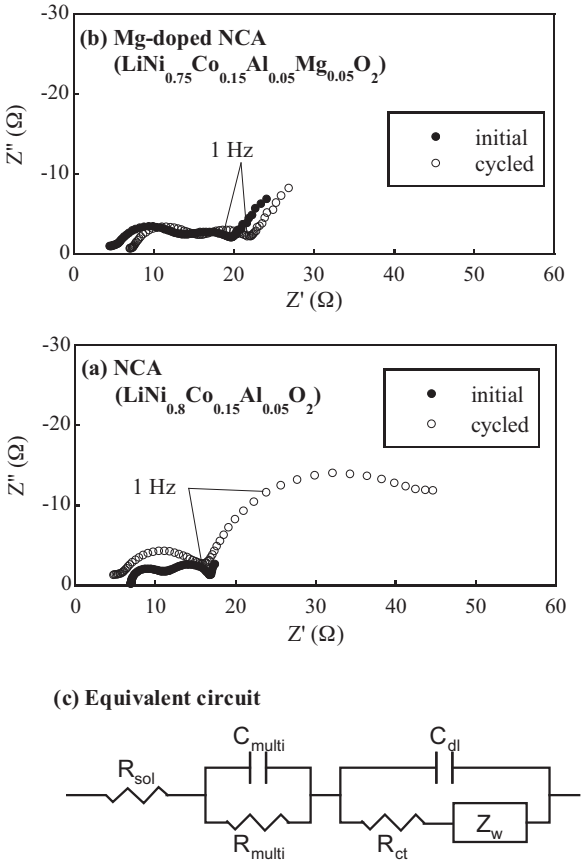

Fig. 1. Nyquist plots of (a) NCA and (b) Mg-doped NCA cathodes, before and after cycling. Data was collected at 20 °C and 3.78 V vs. Li^+/Li using a three-electrode cell, with Li metal counter and reference electrodes. The charge-transfer resistance of cathode was separated by using an equivalent circuit (c).

As can be clearly seen in Fig. 1(a) and (b), the impedance of the NCA cathode increased by a factor of 4.5 after cycling at 70 °C, whereas the impedance of the Mg-doped NCA cathode increased by only 10%.

We constructed an equivalent circuit (Fig. 1(c)) to evaluate the charge-transfer resistance (R_{ct}) of the cathodes. The equivalent circuit comprises the ohmic resistance (R_{sol}) and two RC-parallel circuits, corresponding to each of two successive arcs observed in the Nyquist plots. One of the RC circuits (corresponding to the cathode) includes the Warburg diffusion impedance (Z_w) [41].

Fig. 2(a) and (b) shows the temperature dependence of the reciprocal of the charge-transfer resistance ($1/R_{ct}$) for the two samples, obtained by the equivalent circuit analysis [40]. The activation energies, evaluated from the slopes of the Arrhenius plots, were 61.7 and 66.4 kJ mol^{-1} for the fresh NCA and Mg-doped NCA cathodes, respectively. The activation energies of the charge-transfer resistance of Li-intercalation/deintercalation for $LiCoO_2$ thin film electrodes have been reported to be 60 and 61 kJ mol^{-1}, respectively [41]. In that study, it was concluded that desolvation of Li ions during the charge-transfer reaction was responsible for the relatively large activation energies [42]. The activation energy of the lithium-ion transfer reaction through the graphite/electrolyte interface was also determined to be 53–60 kJ mol^{-1}, and it was concluded that the rate-determining step of the charge-transfer reaction of graphite was also desolvation [43–45]. The present activation energies for the charge-transfer reaction obtained for the $LiNiO_2$-based materials (61.7–66.4 kJ mol^{-1}) are larger than the reported values by a factor of ~10%, though the activation energy depends on the composition of the electrolyte solution and on the composition of the active materials [29,45,46]. Thus, we believe that the rate-determining step for the charge-transfer of NCA and Mg-NCA cathodes is also the desolvation of Li ions from the solvent similar to the previous study.

Fig. 2(a) shows that the activation energy for the charge-transfer of the NCA cathode increased by only 6% after cycling, whereas the geometry factor (the intercept of the straight line, extrapolated to infinite temperature) decreased significantly. This result indicates that the rise in impedance of the NCA cathode was caused by a reduction in the number of active sites for the charge-transfer process. This is consistent with our previous reports because the NiO-like degraded phase (with a nickel valence of +2) increased near the surface of the NCA particles during the cycling test [29,31], and is considered to be inactive towards the charge-transfer reaction. The frequency factor of the charge-transfer reaction of the NCA cathode was thus decreased by charge–discharge cycling.

In contrast, the Arrhenius plot of the charge-transfer resistance for Mg-doped NCA did not vary appreciably with cycling, as shown in Fig. 2(b), suggesting a different microstructural evolution associated with cycling.

3.3. STEM-EELS SI-MCR

Before applying the MCR method to the data, the number of components was assumed to be three or four, judging from our criterion [32]. Typical examples of SI-MCR results for the samples after initial conditioning and after 500 cycles at 70 °C are shown in Fig. 3. Three spectral components are assumed, as in the case of

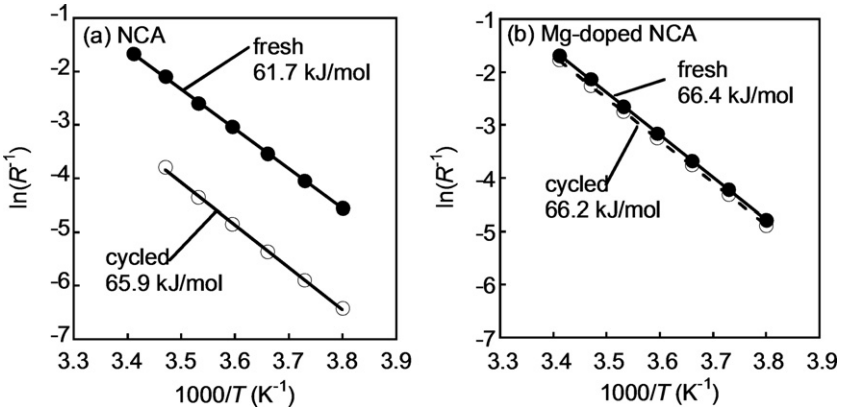

Fig. 2. Temperature dependence of the charge-transfer resistance of (a) NCA and (b) Mg-doped NCA, before and after the cycling test. Activation energies were evaluated from the slopes of Arrhenius plots by the least-squares method, and are noted in the graphs.

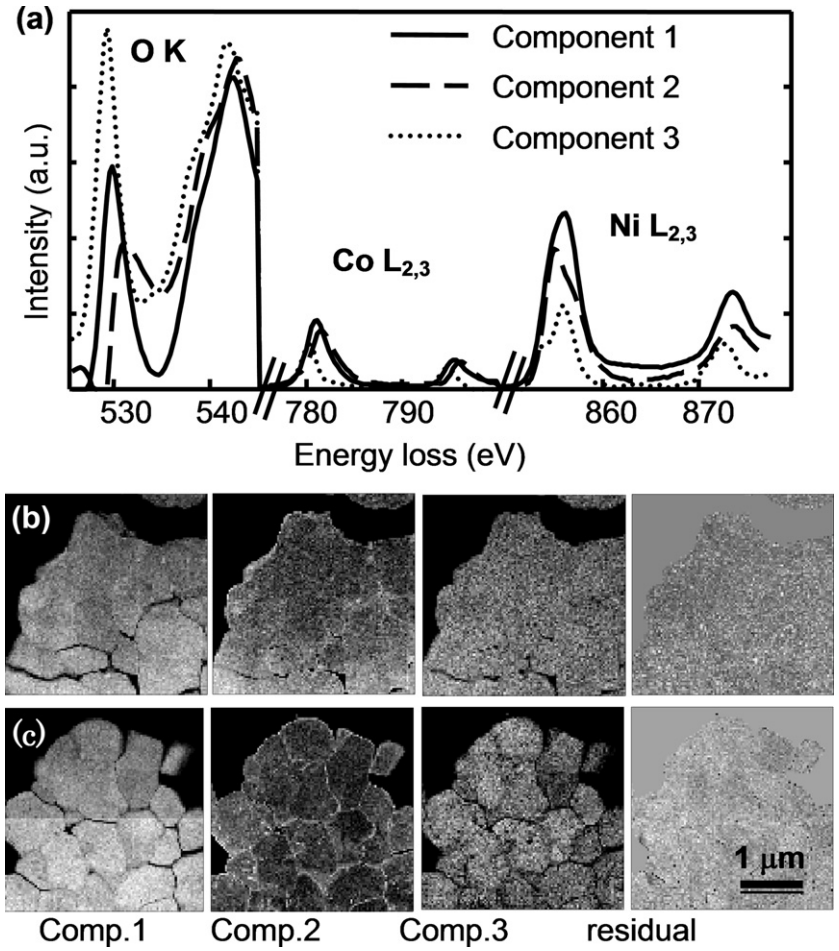

Fig. 3. Three-component STEM-EELS SI MCR analysis results of an Mg-doped NCA cathode before and after cycling at 70 °C. (a) Extracted spectral components common between the samples, before and after cycling. Spatial distribution maps of the spectral and residual components (b) before cycling and (c) after cycling.

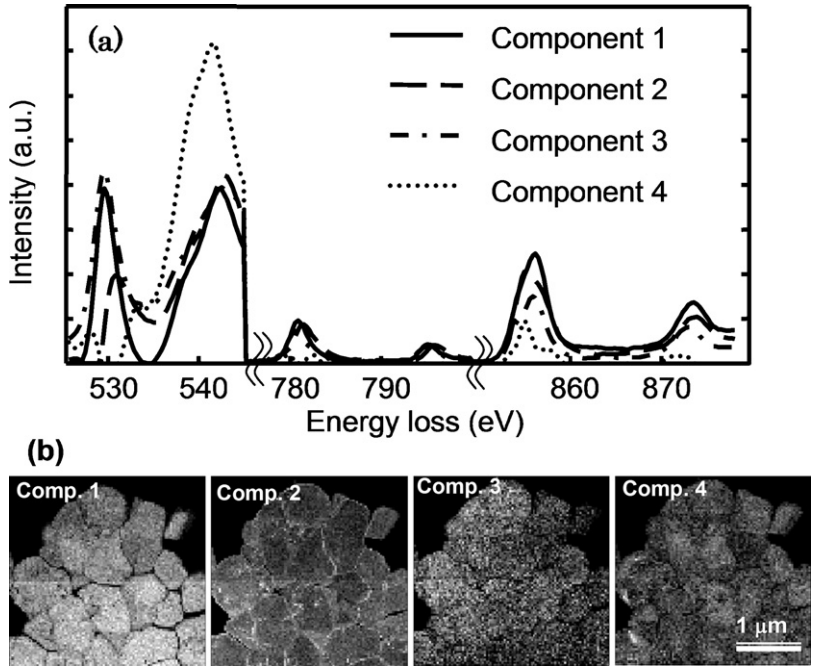

Fig. 4. Four-component STEM-EELSSI MCR analysis results of a Mg-doped NCA cathode before and after cycling at 70 °C: (a) extracted spectral components; (b) spatial distribution maps.

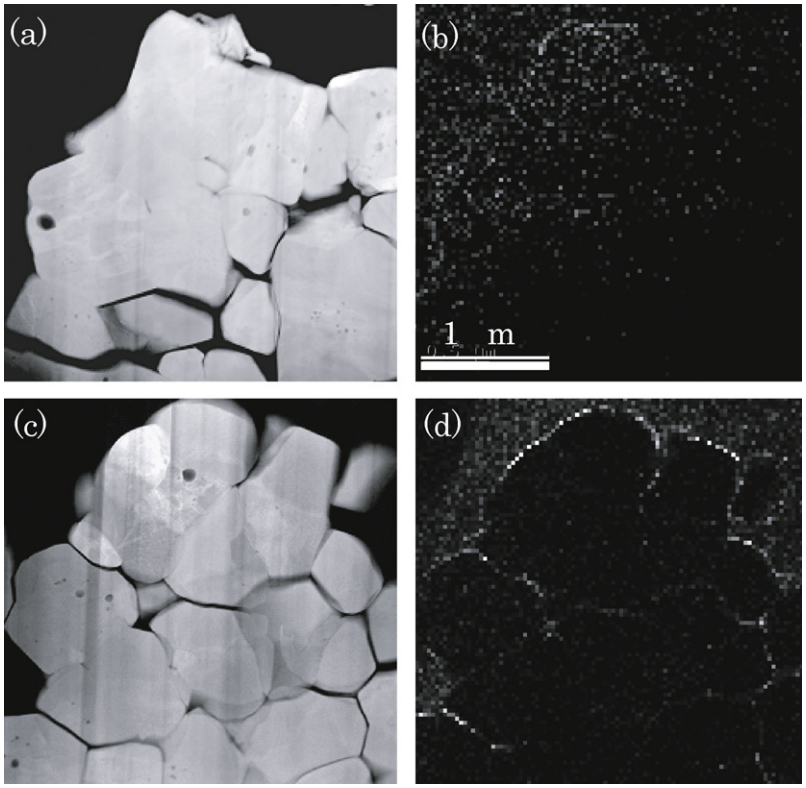

Fig. 5. Annular dark-field images of the Mg-doped NCA cathode sample (a) before and (c) after cycling. Energy filtered images showing fluorine distribution (b) before and (d) after cycling.

our previous report [31]. The two sample types were found to have resolved components in common. As in our previous report [31], the first and third components are assigned from the spectral features to the original phase and the lithium-deficient phase, respectively [31], while the second component, distributed mainly near the surface and grain boundaries of the active material particles, is likely to differ from the original structural phase. Several conclusions can be drawn from these findings. Firstly, the O-K ELNES pre-peak position of component 2 is different from that of the NiO-like phase observed previously [31] (Fig. 3(a)). Secondly, the Ni $L_{2,3}$ ELNES of component 2 is also different from that of the NiO-like phase, displaying an intermediate valency between the divalent and trivalent states judged from the L_3 peak profile and relative L_3/L_2 intensity ratio (the fingerprints of divalent and trivalent Ni-L_3 profiles are presented in Ref. [31] (Fig. 3(a)). Thirdly, the relative concentration of component 2 is not significantly increased after 500 cycles at 70 °C. Finally, the average primary particle size in the cycled sample is smaller than that of the initially conditioned sample.

It is noted that the residual signal after cycling has a weak heterogeneous structure, rather than being random statistical noise, suggesting that another underlying component could be extracted from the data because of the uniqueness of the MCR solutions [30–32]. Thus, for safety, we attempted to apply four-component MCR to the SI dataset of the sample (Fig. 4). The O-K ELNES of the fourth component exhibits features similar to those of the NiO-like phase, and the 2D residuals (not shown) show no appreciable structure, though this component contains some Co, and the relative intensity of Ni-$L_{2,3}$ is small. This component was always uniformly present in the carbon binder regions as well [33]. (In our analysis, the binder regions are usually removed from the dataset.) It is thus reasonable to conclude that this fourth component is due to the damaged surface layer produced during the FIB thinning process, rather than the product phase associated with the charge–discharge reactions.

As in our previous work [33] on undoped NCA cathodes, the correlation between degradation and capacity fade and the increase in resistance with cycling can be investigated by measurement of the average radii of the particles (assuming a spherical particle shape). The results are summarized in Table 2. The increase in the fraction of the product phase induced by cycling was considerably suppressed in the Mg-doped sample, whereas considerable degradation was caused by cycling in undoped samples, as reported in Ref. [33]. The capacity fade of the Mg-doped samples is also roughly explained by the present analysis within the statistical error of the measurement, as shown in Table 2. This result is consistent with the results in Section 3.1.

The NiO-like phase in the undoped NCA samples has been correlated with fluorine distribution [31], and therefore, energy-filtered images were examined using F K ELNES (Fig. 5). Some fluorine was distributed near the surface of the particles, but less than that in the undoped samples. The low-loss region including Li-K ELNES was examined in the same manner as in our previous paper [32]. The MCR method yielded much lesser surface-localized phase in comparison with previous reports, and its spectral profile was too unstable for repeated MCR applications to identify its chemical state. This result corresponds to smaller amount of fluorine and

Table 2
Average particle radius, $\langle r \rangle$, average thickness, $\langle \Delta z \rangle$, standard deviation, σ, and volume fraction, $\Delta V V^{-1}$ of the product phase, roughly estimated from the experimental results for the respective samples of Mg-doped NCA.

	Initial conditioning	70 °C
$\langle r \rangle$ (nm)	470	370
$\langle \Delta z \rangle$ (nm)	50	50
σ (nm)	30	20
$1 - \Delta V/Vc$	0.69(10)	0.63(11)
$\Delta(\Delta V V^{-1}) \times 100$ (%)	–	−9(15)

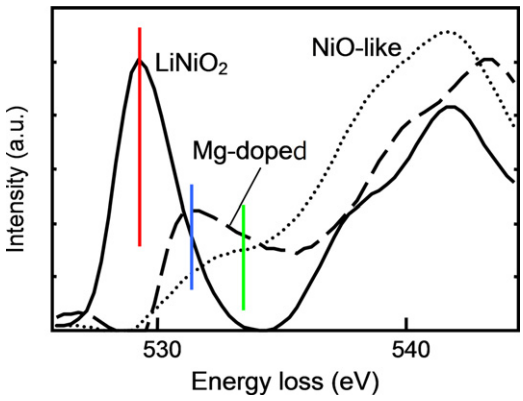

Fig. 6. Three extracted types of O K ELNES by MCR are compared. The pre-peak positions are marked by color solid lines.

lithium fluorides in the surface region of Mg-doped samples, suggesting that the Mg-doped cathode has increased stability against surface reactions with fluorine in the electrolyte.

Phosphorous was also found near the surface regions, though no evolution of the phosphorous distribution was observed upon cycling, as in the case of the undoped NCA [32].

3.4. Theoretical ELNES of O-K

Experimental O-K and Ni-$L_{2,3}$ ELNESs of the initial $LiNiO_2$ phase, the NiO-like phase, and the new spectral feature in the Mg-doped NCA sample (component 2 in Fig. 3(a)) are compared in Figs. 6 and 7(a). As mentioned in the previous section, the pre-peak position of O-K ELNES for the Mg-doped sample is located between $LiNiO_2$ and NiO. In addition, the Ni-$L_{2,3}$ ELNES spectrum of the Mg-doped NCA sample appears to be a summation of the $LiNiO_2$ and NiO spectra. It is thus reasonable to assume that the new chemical state in Mg-doped NCA corresponds to a local change in particle surface chemistry, an intermediate state between the $LiNiO_2$ and NiO-like local atomic configurations, probed by EELS, without changes in structure from the parent material. A candidate that exhibits the red-shift of the oxygen pre-peak could be an under-coordinated transition metal site, such as the tetrahedral site in the spinel structure. A nominal spinel-like composition, $Li_{0.5}NiO_2$, can be locally formed by Li and Ni ions settling on the tetrahedral site (from their original octahedral site) during degradation to the NiO-like phase [33], imposing an intermediate metastable state on the Ni ions. Indeed, the spinel phase has been experimentally observed in a $LiCoO_2$ cathode with a degraded surface [47].

It was difficult to fully reproduce the energy and intensity of the first peak of the $LiNiO_2$ phase, in contrast to the excellent agreement between the experimental and theoretical O-K ELNES for NiO, as shown in Fig. 7(b). This may be attributed to the limited many-body interactions of the O 2p and Ni 3d electrons in these GGA + U calculations. Varying the U_{eff} value did not improve the result. Moreover, the experimental energy between the first peak and the threshold of the main structure at 535 eV (Fig. 6) is approximately 6 eV, which is larger than the GGA + U band gap of 5 eV. The theoretical underestimate of the band gap could be closely related to the incorrect first peak position. To our knowledge, no successful theoretical reproduction of the O-K spectrum of $LiNiO_2$ has been reported. Further theoretical considerations with higher accuracy than GGA + U will be a topic of a future study.

To reproduce the local chemical environment around oxygen in the new phase, the virtual Ni_3O_4 spinel model structure was assumed instead of $Li_{0.5}NiO_2$ to simplify the calculation procedure, since ELNES is mainly affected by first nearest-neighbor coordinated atoms. The O-K ELNES for this structure was calculated according to the same scheme as for the NiO-like phase (see Fig. 7(b)). The energy axis was calibrated by the position of the highest peak around 542 eV. The theoretical O-K ELNES for NiO has already been reported to be in good agreement with experiment [40]. In the intermediate structure, Ni occupies both the tetrahedral and octahedral sites, the different crystal fields of which are reflected in the first O-K ELNES peak, because the oxygen 2p bands are hybridized with the Ni 3d bands. As expected, the first Ni_3O_4 peak (O 2p hybridized with Ni 3d at the tetrahedral site) was at a lower energy than the second peak (O 2p hybridized with Ni 3d at the octahedral site). The relative energy of the first peak was approximately consistent with the experimental spectrum of the intermediate phase for the case of NiO. In this case, the Ni-$L_{2,3}$ ELNES should exhibit an intermediate spectral profile between the trivalent and divalent states, which is consistent with the experimental result.

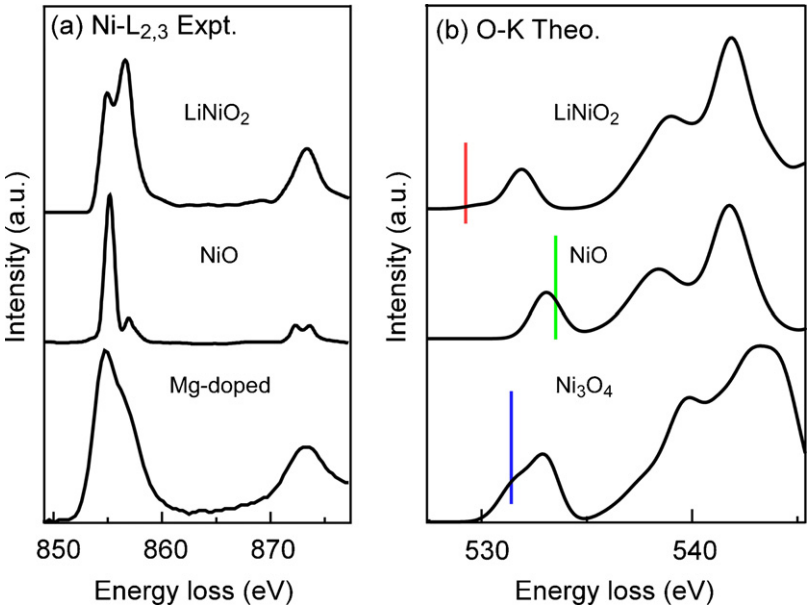

Fig. 7. (a) Experimental Ni $L_{2,3}$ ELNESs. (b) Calculated O K ELNES profiles. The pre-peak positions in the experimental spectra (Fig. 6) are inset as solid color lines.

Our previous paper [35] reported that doped Mg, which occupies the cation sites, reinforces the Ni—O (Li—O) bonding around the dopant. This prevents oxygen elution, resulting in the lattice collapse to the rock-salt structure (NiO-like phase) which is associated with Li deintercalation. The present observation corresponds well to this because Ni at the tetrahedral site can be interpreted as the metastable state instead of further elution of Ni to the electrolytes in undoped cathodes.

4. Conclusions

The degradation of Mg-doped NCA cathode materials upon cycling at elevated temperature was examined by EIS and STEM-EELS SI techniques. The results obtained can be summarized as follows. (1) The capacity fade and increase in internal resistance associated with charge–discharge cycling at 70 °C were significantly suppressed in the Mg-doped NCA cathode. (2) The EIS results suggested that the impedance rise in the cycled NCA cathode was due to the reduction in the number of active sites for the charge transfer process, which is attributable to the formation of the surface degradation phase, as reported in our previous work. Conversely, the Mg-doped NCA cathode exhibited little change in either activation energy or frequency factor. (3) The spatial mapping of the Mg-doped NCA sample showed significantly lesser degradation than the undoped NCA cathode [33] after cycling at 70 °C. The degraded regions of the Mg-doped NCA cathode are suggested to be in an intermediate under-coordinated transition metal state (locally spinel-like), rather than the NiO-like phase seen in undoped NCA. The evolution of this local intermediate structure was significantly suppressed under cycling, resulting in reduced capacity fade and impedance rise compared with those of undoped samples.

Acknowledgment

This work is supported in part by a Grant-in-Aid for Scientific Research (KAKENHI) in Priority Area (#474) “Atomic Scale Modification” from MEXT, Japan.

References

[1] K. Mizushima, P.C. Jones, P.J. Wiseman, J.B. Goodenough, Mater. Res. Bull. 15 (1980) 783–789;
J.B. Goodenough, K. Mizushima, T. Takeda, Jpn. J. Appl. Phys. 19 (1980) 305–313.
[2] M.G.S.R. Thomas, W.I.F. David, J.B. Goodenough, P. Groves, Mater. Res. Bull. 20 (1985) 1137–1146.
[3] J.R. Dahn, U. von Sacken, C.A. Michal, Solid State Ionics 44 (1990) 87–97.
[4] J.R. Dahn, U. von Sacken, M.W. Juzkow, H. Al-Janaby, J. Electrochem. Soc. 138 (1991) 2207–2211.
[5] T. Ohzuku, A. Ueda, M. Nagayama, J. Electrochem. Soc. 140 (1993) 1862–1870.
[6] M. Broussely, F. Perton, J. Labat, R.J. Staniewicz, A. Romero, J. Power Sources 43–44 (1993) 209–216.
[7] C. Delmas, I. Saadoune, Solid State Ionics 53–56 (1992) 370–375.
[8] C. Delmas, I. Saadoune, A. Rougier, J. Power Sources 43–44 (1993) 595–602.
[9] A. Ueda, T. Ohzuku, J. Electrochem. Soc. 141 (1994) 2010–2014.
[10] J.N. Reimers, E. Rossen, C.D. Jones, J.R. Dahn, Solid State Ionics 61 (1993) 335–344.
[11] E. Rossen, C.D.W. Jones, J.R. Dahn, Solid State Ionics 57 (1992) 311–318.
[12] M.E. Spahr, P. Novak, O. Haas, R. Nesper, J. Power Sources 68 (1997) 629–633.
[13] T. Ohzuku, Y. Makimura, Chem. Lett. 30 (2001) 744–745.
[14] T. Ohzuku, A. Ueda, M. Kouguchi, J. Electrochem. Soc. 142 (1995) 4033–4039.
[15] Q. Zhong, U. von Sacken, J. Power Sources 54 (1995) 221–223.
[16] C. Delmas, M. Menetrier, L. Croguennec, I. Saadoune, A. Rougier, C. Pouillerie, G. Prado, M. Grune, L. Fournes, Electrochim. Acta 45 (1999) 243–253.
[17] C. Pouillerie, L. Croguennec, Ph. Biensan, P. Willmann, C. Delmas, J. Electrochem. Soc. 147 (2000) 2061–2069.
[18] C.-C. Chang, J.Y. Kim, P.N. Kumta, J. Electrochem. Soc. 147 (2000) 1722–1729.
[19] S. Madhavi, G.V. Subba Rao, B.V.R. Chowdari, S.F.Y. Li, J. Power Sources 93 (2001) 156–162.
[20] K.K. Lee, W.S. Yoon, K.B. Kim, K.Y. Lee, S.T. Hong, J. Power Sources 97–98 (2001) 308–312.
[21] J.S. Weaving, F. Coowar, D.A. Teagle, J. Cullen, V. Dass, P. Bindin, R. Green, W.J. Macklin, J. Power Sources 97–98 (2001) 733–735.
[22] M. Broussely, P. Blanchard, P. Biensan, J.P. Planchat, K. Nechev, R.J. Staniewicz, J. Power Sources 119–121 (2003) 859–864.
[23] C. Pouillerie, F. Perton, P. Biensan, J.P. Peres, M. Broussely, C. Delmas, J. Power Sources 96 (2001) 293–302.
[24] A. D'Epifanio, F. Croce, F. Ronci, V. Rossi Albertini, E. Traversa, B. Scrosati, Chem. Mater. 16 (2004) 3559–3564.
[25] J. Shim, R. Kostecki, T. Richardson, X. Song, K.A. Striebel, J. Power Sources 112 (2002) 222–230.
[26] C.H. Chen, J. Liu, M.E. Stoll, G. Henriksen, D.R. Vissers, K. Amine, J. Power Sources 128 (2004) 278–285.
[27] Y. Ito, Y. Ukyo, J. Power Sources 146 (2005) 39–44.
[28] M. Broussely, P. Biensan, F. Bonhomme, P. Blanchard, S. Herreyre, K. Nechev, R.J. Staniewicz, J. Power Sources 146 (2005) 90–96.
[29] T. Sasaki, T. Nonaka, H. Oka, C. Okuda, Y. Ito, Y. Kondo, Y. Takeuchi, Y. Ukyo, K. Tatsumi, S. Muto, J. Electrochem. Soc. 156 (2009) A289–A293.
[30] S. Muto, T. Yoshida, K. Tatsumi, Mater. Trans. 50 (2009) 964–969.
[31] S. Muto, Y. Sasano, K. Tatsumi, T. Sasaki, K. Horibuchi, Y. Takeuchi, Y. Ukyo, J. Electrochem. Soc. 156 (2009) A371–A377.
[32] S. Muto, K. Tatsumi, T. Sasaki, H. Kondo, T. Ohsuna, K. Horibuchi, Y. Takeuchi, Electrochem. Solid State Lett. 13 (2010) A115–A117.
[33] Y. Kojima, S. Muto, K. Tatsumi, H. Oka, H. Kondo, K. Horibuchi, Y. Ukyo, J. Power Sources 196 (2011) 7721–7727.
[34] H. Kondo, Y. Takeuchi, T. Sasaki, S. Kawauchi, Y. Itou, O. Hiruta, C. Okuda, M. Yonemura, T. Kamiyama, Y. Ukyo, J. Power Sources 174 (2007) 1131–1136.
[35] K. Tatsumi, Y. Sasano, S. Muto, T. Yoshida, T. Sasaki, K. Horibuchi, Y. Takeuchi, Y. Ukyo, Phys. Rev. B 78 (2008), 045108-1-8.
[36] M. Kerlau, R. Kostecki, J. Electrochem. Soc. 153 (2006) A1644–A1648.
[37] P. Blaha, K. Schwalz, G.K.H. Madsen, D. Kvasnicka, J. Luitz, WIEN2k, An Augmented Plane Wave + Local Orbitals Program for Calculating Crystal Properties (Karlheinz Schwarz, Techn. Universität Wien, Austria), 2001, ISBN:3-9501031-1-2.
[38] G. Kresse, J. Furthmuller, Phys. Rev. B 54 (1996) 11169–11186.
[39] F. Zhou, M. Cococcioni, C.A. Marianetti, D. Morgan, G. Ceder, Phys. Rev. B 70 (2004) 235121-1–235121-8.
[40] H. Kurata, M. Tujimoto, T. Nemoto, S. Isoda, in: Proceedings of the 49th symposium of the Japanese Society of Microscopy, Microscopy 39 (Suppl. 1) (2004) 49.
[41] F. Scholz (Ed.), Electrochemical Methods, 2nd ed., Springer, Berlin, 2010, p. 159.
[42] Z. Ogumi, Electrochemistry 78 (2010) 319–324.
[43] Z. Ogumi, T. Abe, T. Fukutsuka, S. Yamate, Y. Iriyama, J. Power Sources 127 (2004) 72–75.
[44] T. Abe, H. Fukuda, Y. Iriyama, Z. Ogumi, J. Electrochem. Soc. 151 (2004) A1120–A1123.
[45] Y. Yamada, Y. Iriyama, T. Abe, Z. Ogumi, Langmuir 25 (2009) 12766–12770.
[46] K. Xu, J. Electrochem. Soc. 154 (2007) A162–A167.
[47] H. Gabrisch, R. Yazami, B. Fultz, J. Power Sources 119–121 (2003) 674–679.